Journal of Alloys and Compounds 1037 (2025) 182099

Contents lists available at ScienceDirect

Journal of Alloys and Compounds

journal homepage: www.elsevier.com/locate/jalcom

Research article

Investigating the impact of minor alloying on shear transformation zones and strain rate sensitivity in Pd-based bulk metallic glasses via nanoindentation, correlation symmetry analysis and atom probe tomography

S. Khademorezaian [a], M.W. da Silva Pinto [a], M. Peterlechner [a,b], H. Rösner [a,*], S.V. Divinski [a], M. Eusterholz [c,d], G. Wilde [a]

[a] University of Münster, Institute of Materials Physics, Wilhelm-Klemm-Str. 10, 48149 Münster, Germany
[b] Karlsruhe Institute for Technology (KIT), Laboratory for Electron Microscopy (LEM), Engesserstr. 7, 76131 Karlsruhe, Germany
[c] Karlsruhe Institute of Technology (KIT), Institute for Applied Materials – Materials Science and Engineering (IAM-WK), Engelbert-Arnold-Str. 4, 76131 Karlsruhe, Germany
[d] Karlsruhe Institute of Technology (KIT), Karlsruhe Nano Micro Facility (KNMF), Hermann-von-Helmholtz-Platz 1, 76344 Eggenstein-Leopoldshafen, Germany

ARTICLE INFO

Keywords:
Metallic glass
Shear transformation zone
Strain rate sensitivity
Nanoindentation
Minor alloying

ABSTRACT

Minor additions of Co or Fe significantly affect the plastic behavior of the $Pd_{40}Ni_{40}P_{20}$ bulk metallic glass (BMG) (Nollmann et al., 2016). Co enhances plasticity, while Fe addition leads to early catastrophic failure. Structural analyses via variable resolution fluctuation electron microscopy showed that minor alloying profoundly affect the glassy structures beyond the typically 2 nm range (Hilke et al., 2020). Combining nano-mechanical measurements, 4D-STEM angular correlation symmetry analysis, and atom probe tomography (APT), we explore how microalloying impacts structure–property relationships in these BMGs. High-precision nanoindentation revealed two populations of shear transformation zones (STZs), each with fewer than 100 atoms. The alloy with higher plasticity had smaller STZs, whereas the less ductile alloy showed larger STZs. All samples exhibited negative strain rate sensitivity, with the Fe-containing alloy showing the highest. 4D-STEM analysis indicated increased 5-fold symmetry in the Fe-containing alloy, whereas the Co containing BMG displayed reduced 5-fold symmetry similar to the amount of 4- and 6-fold symmetries. APT mass spectra showed no oxygen species, ruling out oxidation effects. Clustering analysis of nearest-neighbor atom distributions indicated no significant Fe–Fe or Co–Co clustering, suggesting uniform dispersion. Overall, these findings shed light on how microalloying influences the microstructure, strain rate sensitivity, and macroscopic plasticity in BMGs, advancing our understanding of deformation mechanisms in BMGs.

1. Introduction

Understanding the response of metallic glasses to externally applied mechanical stresses has been one of the fundamental and particularly challenging aspects of metallic glasses (MG) research. MGs exhibit many significant advantages, such as high strength, extended elasticity, and high wear resistance. However, the lack of plasticity at temperatures well below the glass transition, especially under tension, has been limiting their use [1]. Significant efforts have been made to improve the plasticity of MGs with minor alloying, emerging as a robust approach to induce substantial improvements in glass-forming ability, thermal stability, and mechanical properties of MGs [2–9].

The accepted description of the mechanism behind the plastic deformation of MGs is rooted in the original works of Argon [10–12], Spaepen [13] and Falk and Langer [14]. The model that has been developed from these approaches suggests that plastic deformation occurs via rearrangement of local atomic regions, also referred to as STZ that undergo transformation under applied shear stress. STZs are understood to be basic units that accommodate shear, thus bearing similarity to dislocations in crystalline materials. Driven by the idea of local events of cooperative shearing, Johnson and Samwer introduced a cooperative shear model (CSM) [15] based on the concept of inherent states and potential energy landscapes [16,17]. The CSM model predicts the mechanical behavior of BMGs to be closely linked to the volume of the STZ.

Direct experimental observations of the STZs are hindered by their transient nature, which makes these entities distinct from dislocations

* Corresponding author.
E-mail address: rosner@uni-muenster.de (H. Rösner).

https://doi.org/10.1016/j.jallcom.2025.182099
Received 29 April 2025; Received in revised form 23 June 2025; Accepted 4 July 2025
Available online 16 July 2025

in a crystalline material. However, recent advancements in nanoindentation have provided the possibility to indirectly probe the activation of STZs. The nanoindentation load–displacement curves for MGs often exhibit a sudden burst of displacement or a load drop in load- or displacement-controlled modes, respectively, commonly referred to as pop-in [18–22]. After pioneering studies on pop-in behavior and serrated deformation in the 1990s [23–26], especially the analysis of the first pop-in during mechanical loading, which denotes the onset of plastic deformation in the material, has become the focal point of numerous studies [27–34]. The progression of macroscopic plasticity under continuously applied compressive or shear stresses occurs through mesoscopic 2D-like defects that are termed shear bands. It is worth noting that a similar coalescence of defects has also been observed during creep experiments [35]. According to recent atomistic studies [36,37], STZ percolation leads to shear band formation through a process involving the interconnected growth and organization of STZs within the material. This process is facilitated by the interaction of two key units: the STZs themselves and vortex-like structures, which are characterized by rotational deformation. The dual STZ-vortex mechanism suggests that the vortical structures promote the alignment and connectivity of STZs. As more STZs percolate, forming a continuous network, they create a localized shear pathway—a narrow zone of intense plastic deformation.

At this point, we would like to clarify the terminology of glass deformation that is applied in the present paper. The first pop-in has been shown to occur often at rather low strain values [38,39], commonly associated with the macroscopic elastic regime. As pop-ins are related to local irreversible structural rearrangements, it is in fact not an elastic response per se [40]. In the macroscopic plastic regime of glass deformation (under compression or shear), localization via shear band formation and shear band activation occurs at temperatures that are well below the glass transition. Thus, the terms “elastic” and/or “plastic” response need to be taken with caution when the response function of metallic glasses to an externally applied mechanical stress is concerned. In the same context, the terms “plasticity” and “brittleness” are applied to distinguish macroscopic catastrophic failure at small strains (“brittleness”) from macroscopic permanent shape change under an applied mechanical load (compression or shear) without immediate failure (“ductile”), even though localization of deformation (and associated shear softening) occurs nevertheless. In this contribution, we shall use these accepted terms for the sake of clarity of the presentation and to signify the correlation with the macroscopic response of the material.

To gain a deeper understanding of the structural factors influencing the mechanical behavior of pristine Pd-based model bulk metallic glasses (BMGs) and their variants modified through minor alloying, this study employs nanoindentation, atom probe tomography (APT), and 4D-STEM. These techniques are integrated to elucidate the relationship between microstructural features and the observed mechanical properties.

2. Experimental procedure

2.1. Alloy fabrication and characterization

The BMG master alloy of $Pd_{40}Ni_{40}P_{20}$ was synthesized using copper mold casting in a purified argon atmosphere with dimensions of 10 × 30 × 1 mm^3 in a cuboid form. The alloy had been fabricated using Pd plates and Ni_2P ingots, all with purities higher than 99.999%. The components were alloyed and pre-melted two times up to 1100 K, once with B_2O_3 for further purification, as described in [41–43]. The master ingots of the ternary $Pd_{40}Ni_{40}P_{20}$ material were subsequently alloyed by minor additions of 1 at.% Co or Fe. Co and Fe have been selected as minor alloying additions due to their similarity with Ni, which is one of the three base components of the pristine glass. With this choice, biasing the material through strong local variations of electron negativity or electron configurations is avoided.

The X-ray amorphous structure of the samples was verified with a Siemens D5000 X-ray diffractometer using Cu K_α radiation. Measurements of the glass transition temperatures and the crystallization enthalpies by differential scanning calorimetry (Mettler DSC 3) confirmed the absence of detectable crystalline fractions in all samples.

2.2. Nanoindentation measurements

For the nanoindentation tests, samples were polished on both sides to achieve plane-parallel specimens. The indentation surface was then further polished to a mirror finish (Struers OP-U, 40 nm particle size). Instrumented nanoindentation tests were conducted at room temperature using a FT-NMT04 IN-SITU SEM Nanoindenter (FemtoTools) equipped with a Berkovich diamond tip. The stiffness of the device has been calibrated by indentation experiments on a standard fused silica sample. The readout precision of the nanoindentors' positions was better than 50 pm in z direction and the noise with respect to the force was less than 0.5 nN (5×10^{-10} N).

Nanoindentation measurements were conducted in load-controlled mode at a constant loading rate of 5 μN/s to the maximum load of 1 mN for the detection of the first pop-in event, and in displacement-controlled CSM mode to evaluate the strain rate sensitivity (SRS) to a maximum displacement of 200 nm.

The tip approach step was made slowly and with a similar displacement speed as the actual nanoindentation measurements to avoid a load jump at the first tip contact. The threshold for the contact detection was set to 2 μm. For the strain rate sensitivity measurements, strain rates of 0.5, 0.05, and 0.005 s^{-1} were used.

2.3. 4D-STEM investigation

An analysis of angular symmetry correlations in electron diffraction has been conducted. For this purpose, the local symmetry information has been extracted from individual nanobeam diffraction patterns of the micro alloyed samples. These patterns were obtained through 4D-STEM using a direct electron detector [44]. Electron-transparent transmission electron microscopy (TEM) samples were prepared by electropolishing with a BK-electrolyte [45] at 16.5 V and −20 °C, employing a Tenupol 5 electropolishing device manufactured by Struers (Denmark).

Prior to loading into the microscope, the samples were plasma cleaned for 90 s in an Ar + O_2 mixture to remove organic contaminants. We utilized a Thermo Fisher Scientific FEI Themis 300 microscope operating at 300 kV in scanning transmission electron microscopy (STEM) mode to investigate the samples' amorphous structures. High-angle annular dark-field scanning transmission electron microscopy (HAADF-STEM) combined with energy-dispersive X-ray spectroscopy (EDS) was employed to analyze the chemical composition.

Nanobeam Diffraction Patterns (NBDPs) were acquired using a parallel coherent probe with a diameter of (1.26 ± 0.02) nm measured at FWHM and a semi-convergence angle of 0.6 mrad in microprobe mode. The probe current was measured at 21 pA, with a camera length set to 245 mm. Individual NBDP maps were collected using a Dectris pixelated detector with a resolution of 512 × 512 pixels, and an exposure time of 100 ms was employed. The diffraction patterns were recorded at a grid of 300 nm × 300 nm size, the positions spaced 6 nm apart to minimize overlap, resulting in a total of 2500 diffraction patterns for analysis. The open source PyXem library, which provides a wide array of 4D-STEM data analysis routines [46–48], was utilized for data processing and evaluation as described in detail by Huang et al. [49].

Angular correlations were determined by extracting the so-called four-point angular auto-correlation function (ACF) from individual NBDP as follows:

$$C(k,\Delta) = \frac{\left\langle I(k,\phi)I(k,\phi+\Delta)_\phi \right\rangle - \left\langle I(k,\phi)\right\rangle_\phi^2}{\left\langle I(k,\phi)\right\rangle_\phi^2}, \quad (1)$$

Here, Δ represents the correlation angle, and $I(k,\phi)$ denotes the diffraction intensity corresponding to the scattering vector k and azimuthal angle ϕ. Next, the function $C(k,\Delta)$ was Fourier transformed with respect to the azimuthal angle ϕ, resulting in the angular power spectrum $\widehat{C}(k,n)$, where n is the corresponding Fourier harmonic. The n-fold rotational symmetry of a structure, which diffracts at a specific k, can then be determined from the Fourier amplitude of $\widehat{C}(k,n)$.

For each pixel in the NBDP series, we computed the angular correlations for both four-, five- and six-fold symmetries at the k-values aligned with the first amorphous ring in the diffraction pattern using the Python package pyxem [46]. These particular symmetries were selected because the four- and six-fold rotational symmetries are associated with more crystal-like structures found in metallic glasses [50], while the five-fold rotational symmetries correspond to icosahedral-like arrangements [51]. The spatial distribution of these rotational symmetries can subsequently be visualized on a pixel-by-pixel basis through the symmetry maps, where the chosen symmetry coefficient is plotted for each acquired NBDP. Further details on this procedure can be found in the Supplementary Material (see Angular Correlation Microscopy (ACM) section).

The direct results from PyXem yield symmetry maps that, in this case, are nearly spatially homogeneous (see Supplementary Material Fig. S1). In addition, a direct comparison of intensities from the symmetry maps may not be reliable because of the residual intensities contributing to each histogram. To facilitate a more accurate comparison between the maps of different symmetry orders, the intensity histogram can be utilized to estimate the actual intensity distribution. For this purpose, a Gaussian kernel density estimate is used, defined as:

$$f(x) = \frac{1}{N_p h}\sum_{i=1}^{N_p} K\left(\frac{x-x_i}{h}\right), \tag{2}$$

where N_p is the number of data points, and x represents the linearized intensity. The kernel, as mentioned above, is a Gaussian function of the form $K(u) = \frac{1}{\sqrt{2\pi}}\exp\left(-\frac{u^2}{2}\right)$. Here, u is the standardized distance between the estimated point at x and any other data point x_i, calculated as $\frac{x-x_i}{h}$, where h is a predetermined bandwidth parameter.

2.4. Atom probe tomography

Specimens for atom probe tomography (APT) analyses were prepared with a conventional lift-out method [52] in an Auriga 60 scanning electron microscope (SEM) equipped with a focused Ga ion beam (Zeiss AG, Germany). The experiments were performed in a LEAP 4000X HR (Cameca Instruments, Madison, WI, USA) in voltage mode with 50 kHz pulse frequency, 20 % pulse fraction, 40 K base temperature, and a detection rate of 0.3%. Data reconstruction and analysis were done using the software package AP Suite 6.3 (Cameca Instruments).

3. Results

Inspired by the CSM model [15], two distinct nanoindentation measurements are reported to estimate the size of the STZ: (i) a statistical method of analyzing the pop-ins and (ii) strain rate jump tests. However, strain rate jump tests have been shown to have restrictions when the SRS is negative, which is the case for most BMGs [53–57].

For shallow indentation, the blunting of the tip makes it possible to approximate the tip as spherical. The tip radius can be estimated from the calibration of the tip function to be of the order of 25 nm. Therefore, the elastic response of the material can be predicted according to isotropic continuum elasticity, using the Herzian law for mechanical contact [58],

According to Schuh and Lund [28] the cumulative distribution of STZ nucleation events or pop-ins as a function of the instantaneous shear stress, τ, beneath the indenter tip, $f(\tau)$, can be expressed as:

$$f = 1 - \exp\left[\frac{kTN_0}{\dot{\tau}V^*}\cdot\exp\left(-\frac{\Delta F^*}{kT}\right)\cdot\exp\left(\frac{\tau V^*}{kT}\right)\right], \tag{3}$$

where T is the temperature, N_0 is the "attempt frequency" of STZ nucleation events [28], k is Boltzmann's constant, ΔF^* is the activation barrier, V^* is the activation volume, and $\dot{\tau}$ is the shear stress rate (which is kept constant for measurements performed at a constant loading rate).

The shear stress of the first pop-in can be associated with the maximum shear stress τ_{max} beneath the indenter. For a spherical indenter τ_{max} is given as:

$$\tau_{max} = 0.31\left(\frac{6E_r^2P}{\pi^3R^2}\right)^{\frac{1}{3}}. \tag{4}$$

P is the load at the first pop-in, R is the indenter radius, and E_r is the effective modulus of the indenter tip–sample system [59].

As shown in Fig. 1(a), under identical experimental conditions, τ_{max} is distributed over a range of about 1.5 to 4 GPa. Both minor alloyed samples show higher values of τ_{max} than the ternary master alloy. This indicates a more pronounced intrinsic spatial heterogeneity in the plastic deformation response of the minor alloyed samples.

Besides this intrinsic heterogeneity it must be mentioned, that indents at different positions and in different samples were made to test and exclude heterogeneities on the μm or even mm scale. Moreover, at slow deformation rates the detection of pop-in events works best. For that reason, only the results of one strain rate are presented and discussed here.

By using a linear least-square fit to the plot of $\ln\left[\ln(1-f)^{-1}\right]$ vs. τ, the activation volume V^* can be obtained directly from the slope of the plot,

$$\ln\left[\ln(1-f)^{-1}\right] = \left[\frac{\Delta F^*}{kT} + \ln\left(\frac{kT}{V^*\dot{\tau}}\right)\right] + \left(\frac{V^*}{kT}\right)\tau. \tag{5}$$

As suggested by Pan et al. [60], the STZ volume, Ω, is given by

$$\Omega = \frac{\tau_C}{6R_fG_0\gamma_C^2\zeta(1-\frac{\tau}{\tau_C})^{1/2}}V^*. \tag{6}$$

Here R_f is the so-called "fold ratio", R_f varies from 1/4 to $\pi^2/32$ as τ decreases from τ_C to 0 [15]; γ_C is the yield strain; G_0 is the shear modulus of the unstressed glass; τ_C is the threshold shear resistance at 0 K; ζ is a correction factor arising from a matrix confinement of STZs and $\zeta \approx 3$ [11].

Johnson and Samwer [15] suggested the following semi-empirical expression for the estimation of τ_C:

$$\frac{\tau_C}{G_0} = \gamma_{C0} - \gamma_{C1}\left(\frac{T}{T_g}\right)^M, \tag{7}$$

where $\gamma_{C0} = 0.036$, $\gamma_{C1} = 0.016$, $M = 0.62$ and T_g is the glass transition temperature.

Eqs. (5)–(7) are used in the present analysis. After evaluating the volume Ω of the STZ and considering a dense-packed hard-sphere model with an average sphere radius of $r_0 = \left(\sum_{i=1}^{N} A_i r_i^3\right)^{1/3}$, the number of atoms composing the STZ can be estimated, too. Here A_i and r_i are the atomic fractions and the radius of each component i. The calculated average atomic radii for the three compositions are almost identical, $r_0 = (0.128 \pm 0.001)$ nm.

Using Eq. (3), the fits do not adequately represent the distribution of STZ nucleation events, particularly at lower and higher τ_{max} values as shown in Fig. 1(a). In Fig. 1(b), the $\ln[-\ln(1-f)]$ vs. τ_{max} dependencies reveal two distinct branches following approximately linear regressions. The corresponding R^2 factors for both branches exceed 0.98.

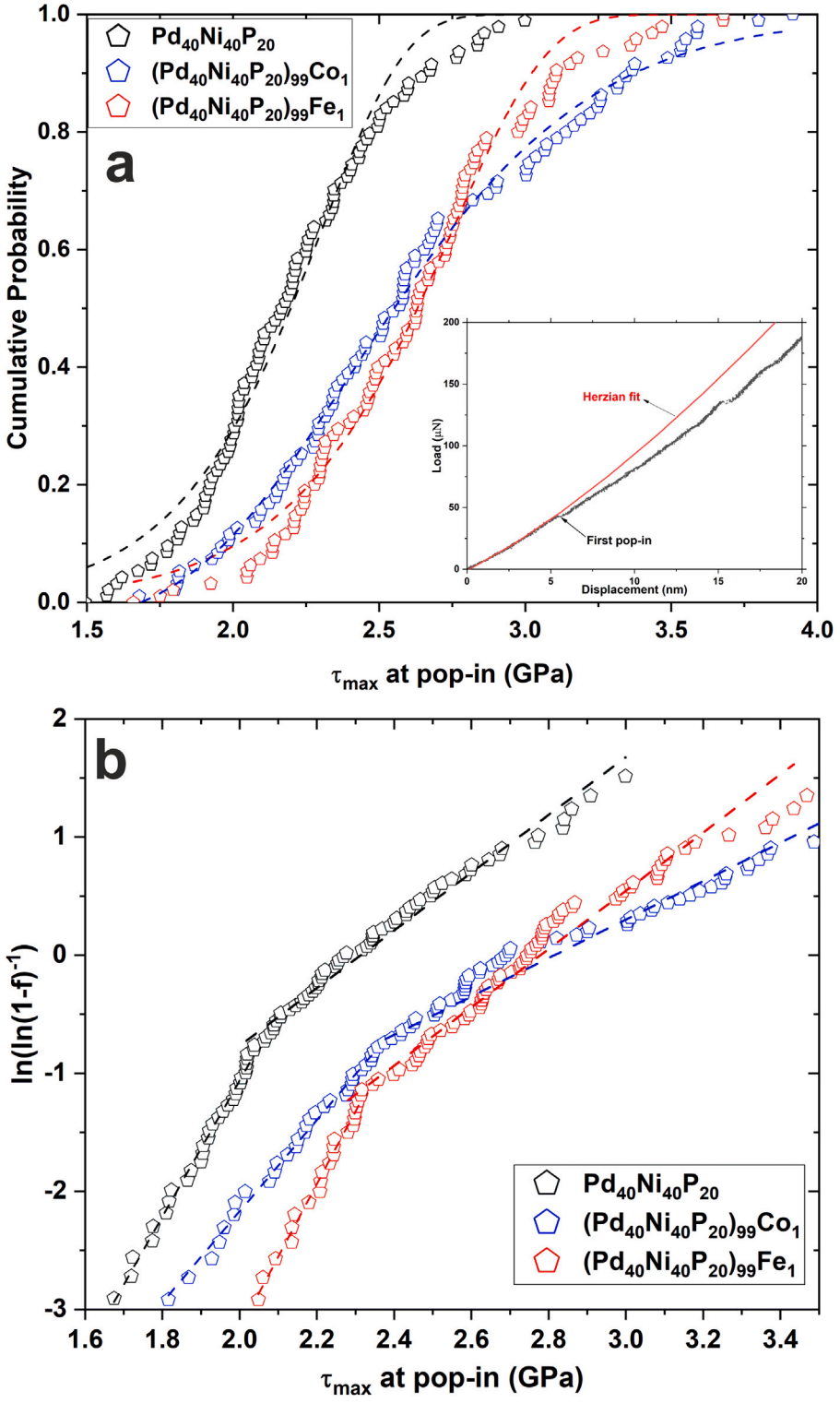

Fig. 1. (a) The cumulative probability distribution f of the maximum shear strength τ_{max} for the three compositions under investigation. (b) Two linear fits to the $\ln\left[\ln(1-f)^{-1}\right]$ vs. τ_{max} dependence demonstrating the existence of two separate contributions with different slopes. To achieve accurate fitting, the lowest and highest 5% of the force measurements are excluded. This approach addresses the influence of surface roughness and contact initiation at low forces as well as multiple contact events occurring at high forces.

By employing linear approximations, the activation volume, V^*, and the STZ volume values, Ω, were estimated for the three alloys and are listed in Table 1. These results align well with the known STZ volumes in various MGs, typically ranging between 0.2 nm^3 and 0.8 nm^3 [34,61–64].

It is worth noting that the slope of the linear regression in Fig. 1(b) changes abruptly. The τ_{max} value at this slope change can be considered as a critical value, τ_C. Below this threshold, the activation volumes denoted as V_1^* are significantly larger than the activation volumes V_2^* at higher τ_{max} values. Initially, it may seem counter-intuitive that lower τ_{max} values activate larger STZs. One hypothesis is that applied stresses, alongside the activation of pre-existing STZs, may alter atomic configurations in a way that smaller STZs are initiated or become active. Additionally, the possibility of percolation of multiple even

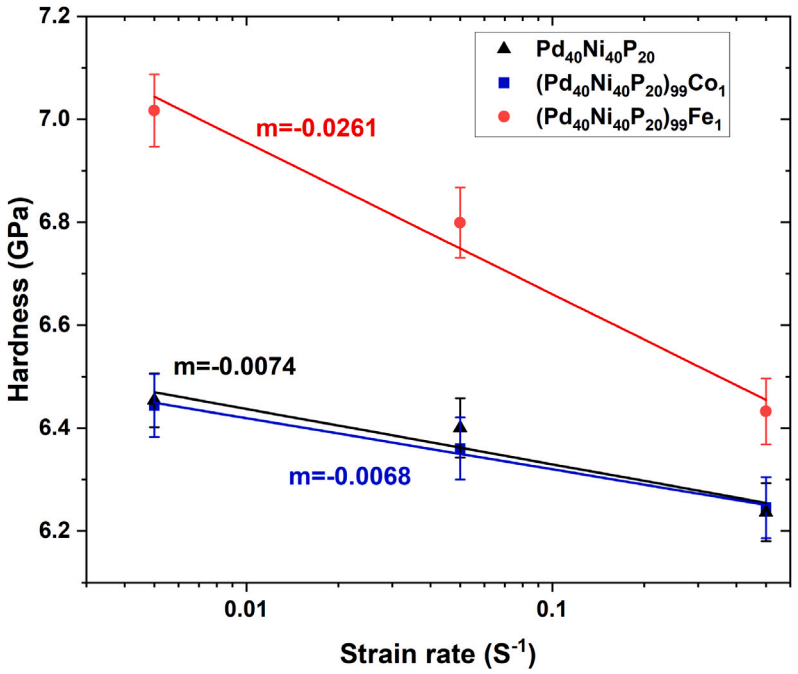

Fig. 2. The strain rate sensitivity exponent m determined for the three compositions of pristine and minor alloyed $Pd_{40}Ni_{40}P_{20}$.

Table 1
Activation and STZ volumes extracted from the statistical analysis of the first pop-in.

Material	Activation volume V^* (nm^3)		STZ volume Ω		No. of atoms in STZ	
	1st	2nd	1st	2nd	1st	2nd
$Pd_{40}Ni_{40}P_{20}$	0.0236	0.0099	0.797	0.335	89	38
$(Pd_{40}Ni_{40}P_{20})_{99}Co_1$	0.0157	0.0066	0.531	0.223	61	25
$(Pd_{40}Ni_{40}P_{20})_{99}Fe_1$	0.0252	0.0111	0.853	0.377	97	43

smaller STZs near the threshold stress cannot be ruled out. It can be inferred that micro alloying raises the threshold value. For instance, the τ_C value is 2.03 GPa for the ternary alloy, increasing to 2.34 GPa for $(Pd_{40}Ni_{40}P_{20})_{99}Co_1$ and 2.31 GPa for $(Pd_{40}Ni_{40}P_{20})_{99}Fe_1$.

Here, a correlation between $\ln[-\ln(1-f)]$ and τ_{max} with the mechanical response can be made. The sharper change in slope and the associated alterations in activation volume observed for $(Pd_{40}Ni_{40}P_{20})_{99}Fe_1$ at τ_C, contrast with the more gradual changes seen in $Pd_{40}Ni_{40}P_{20}$ and $(Pd_{40}Ni_{40}P_{20})_{99}Co_1$. It is suggested that in more ductile metallic glasses, the activation of smaller STZs is more pronounced, leading to a more homogeneous progression and smaller stress fields. Conversely, the more brittle alloys exhibit a larger activation volume, creating larger stress fields and promoting an almost abrupt activation of smaller STZs above τ_C, ultimately resulting in a catastrophic-like propagation of fewer dominant shear bands.

The approach proposed above differs from other approaches that assume a certain distribution of activation volumes (STZ volumes) within a sample. For instance, the initiation of pop-ins has been proposed to exhibit a bimodal distribution [65], indicating the presence of two distinct families of events with varying activation volumes and corresponding activation barriers.

Other models, like the 3-parameter Weibull model, have also been employed to characterize the distribution of τ_{max} [22,66,67]. In this scenario, the concept of stresses necessary for shear bands to form along different stress trajectories has led to a bimodal distribution of τ_{max} [67]. The key finding is that this bimodal distribution becomes more pronounced under high loads and loading rates, likely due to the influence of a large spherical indenter radius that amplifies the deformation volume. However, our current investigation focuses on significantly smaller deformed volumes due to a smaller tip radius, lower applied forces, and lower loading rates. The continued activation of new STZ families under these conditions suggests that the observed effects are not solely driven by the factors emphasized by Nag et al. [67].

3.1. Strain rate sensitivity

The strain rate sensitivity (SRS) provides valuable information about the plasticity and the deformation behavior of a given material.

Three methods have been widely used to measure the SRS:

(i) measurements at constant loading rate (CRL) until the tip displacement rate reaches a nearly constant value [68];
(ii) measurements at constant strain rate (CSR) [69] by applying an exponential load-time function;
(iii) a strain rate jump test in which the strain rate is changed in immediate steps to measure the resulting hardness change.

The strain rate jump method has three principal drawbacks. First, the hardness obtained is from a deformed structure. Second, the pile-up effect would also affect the SRS values as reported by Bhattacharyya et al. [55] and third, strong serrations at low strains create large discontinuities of hardness values leading to large uncertainties. For the CRL method, the strain rate changes continuously during the loading segment. Therefore, the CSR method has been applied here.

In displacement-controlled self-similar indentation, the strain rate is defined as $\dot{\epsilon} = (1/h)dh/dt$ and the SRS is determined as :

$$m = \frac{\partial H}{\partial \dot{\epsilon}}. \tag{8}$$

The results of our investigation are shown in Fig. 2 and Table 2. For all compositions, negative values of m are obtained. The m value for the Co minor alloyed system resembles that of the ternary master alloy, while the strain rate sensitivity for the alloy with minor Fe addition shows a significant deviation from the value of the pristine BMG.

Table 2
Values of m and average hardness for the three compositions.

	Strain rate sensitivity m	Average hardness (GPa)
$Pd_{40}Ni_{40}P_{20}$	-0.0074 ± 0.0002	6.24 ± 0.62
$(Pd_{40}Ni_{40}P_{20})_{99}Co_1$	-0.0068 ± 0.0001	6.23 ± 0.55
$(Pd_{40}Ni_{40}P_{20})_{99}Fe_1$	-0.026 ± 0.0001	6.72 ± 0.71

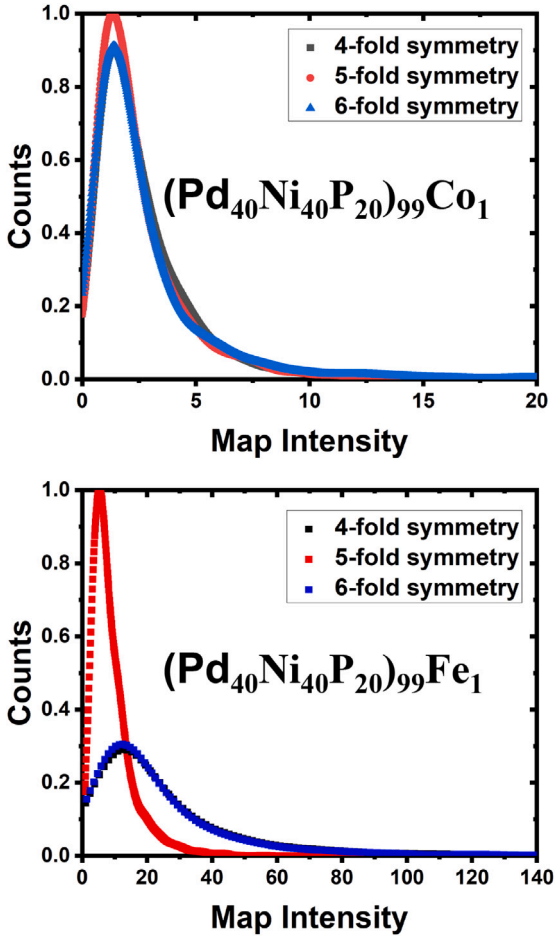

Fig. 3. Analysis of the amorphous structure through angular symmetry correlation analyses by utilizing local symmetry information extracted from individual nanobeam diffraction patterns of the micro alloyed samples. A distinctly higher degree of 5-fold symmetry is observed in $(Pd_{40}Ni_{40}P_{20})_{99}Fe_1$ (bottom) whereas the 5-fold symmetry in $(Pd_{40}Ni_{40}P_{20})_{99}Co_1$ (top) tends to align more closely with 4- and 6-fold symmetries. Note that the peak heights have been normalized to the maximum peak.

3.2. Angular correlation microscopy

One effective method for assessing local glass structure and rotational symmetry in amorphous materials is through electron nanodiffraction. This technique utilizes a parallel nano-sized electron beam to probe a small volume of atoms within the sample. The structural information is captured in the diffraction pattern, with local arrangements producing Bragg-like coherent speckles. For the purpose of analyzing dominant local symmetries, angular correlations were computed by extracting the angular correlation function from individual NBDP, as described in the experimental section. Further details are provided in the Supplementary Material. The main results are illustrated in Fig. 3, emphasizing the distinctions between the two micro alloyed alloys. Specifically, the Fe containing alloy demonstrates an enhanced 5-fold symmetry relative to 4- and 6-fold symmetries, whereas the more deformable Co containing BMG [7,70] displays the fraction of 5-fold symmetry more aligned with the fractions of 4- and 6-fold symmetries.

3.3. Atom probe tomography

First of all, the APT profiles displayed in the Supplementary Material (see Fig. S7) confirm the chemically homogeneous states of all alloys and their precise alignment with the nominal compositions.

Furthermore, for all alloys, no signs related to oxygen containing species exist in the APT mass spectra. Our clustering analysis, utilizing nearest-neighbor distributions compared with a randomized system, eliminates the possibility of any cluster formation, particularly those related to Fe–Fe or Co–Co clusters, as illustrated in Fig. 4. The Pearson contingency coefficient [71] is for both, Fe in $(Pd_{40}Ni_{40}P_{20})_{99}Fe_1$ and Co in $(Pd_{40}Ni_{40}P_{20})_{99}Co_1$, below 0.01, underscoring the case for a homogeneous distribution.

4. Discussion

It is worth noting that these three alloys have been extensively characterized in prior studies concerning their plastic response — via compression and 3-point bending tests — as well as their calorimetric behavior using differential scanning calorimetry (DSC), mechanical properties such as Poisson's ratio, and medium-range order (MRO) using fluctuation electron microscopy [7,70].

The relaxation spectrum of glassy solids, particularly the presence of a rapid secondary relaxation process occurring at temperatures well below the glass transition temperature (T_g), has been closely linked to their deformation behavior [72,73]. This secondary relaxation, characterized by a low activation energy (0.3–0.6 eV), provides valuable information on the atomistic mechanisms that differentiate brittle failure from plastic flow in various temperature regimes [74,75].

Thermal relaxation near the glass transition temperature which is referred to as α relaxation usually leads to embrittlement [76–78]. To better understand how thermal relaxation and composition influence room-temperature plasticity in metallic glasses, a model based on the relationship between T_g and a critical fictive temperature (T_f) has been proposed [79]. As defined by Tool and Eichlin [80] the fictive temperature quantifies the relaxation state of a glass and, within free volume models, reflects the relative amount of free volume retained in the structure.

Furthermore, it has been demonstrated that multiple shear banding events — leading to enhanced plasticity — can be triggered by elastic pre-loading [81–84] or cryogenic cycling [84,85], which can also induce an unusual brittle-to-ductile transition in the material's malleability. These phenomena likely originate from spatial heterogeneities [75,83,86] introduced by thermal, elastic, or plastic stimuli, which significantly alter or lower the energy barriers for shear transformation zone (STZ) activation, thereby increasing the frequency of STZ events during deformation.

The calorimetric characterization by DSC [7] has been conducted in conjunction with the fictive temperature concept to assess the influence of minor alloying elements. Interestingly, despite their markedly different mechanical behaviors, the absolute fictive temperatures of the as-quenched states for the ternary and Fe-containing alloys were very similar. This suggests that the total amount of frozen-in free volume during vitrification may be less critical to the mechanical properties of bulk metallic glasses than its local distribution within the atomic structure.

Additionally, our prior study [7] revealed that the Poisson's ratios for all three alloys were consistently around 0.4, indicating no direct correlation between the mechanical behavior and the measured Poisson's ratio in these materials.

Employing the higher nearest-neighbor distributions for the APT analysis, Section 3.3, enhances our understanding of the clustering phenomena present within the system [87]. Critically, the present discussion avoids biases arising from structural cluster formation of Co or Fe as a result of micro alloying. This allows the mechanical and

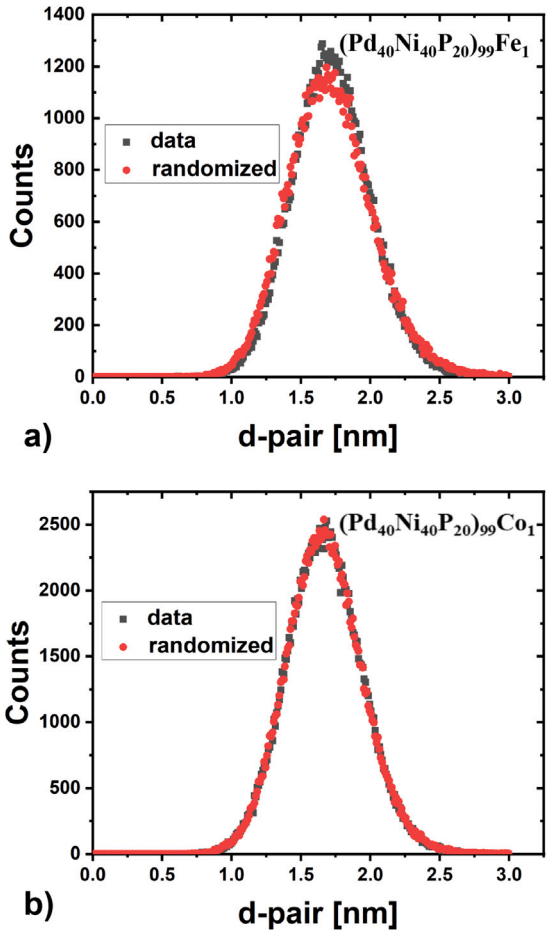

Fig. 4. 5th nearest-neighbor distributions for (a) Fe–Fe in $(Pd_{40}Ni_{40}P_{20})_{99}Fe_1$ and for (b) Co–Co in $(Pd_{40}Ni_{40}P_{20})_{99}Co_1$, which are compared with randomized nearest neighbor distributions (red curves).

microstructural analysis to focus exclusively on intrinsic mechanisms, such as STZ and MRO.

The present work traces the initial deformation behavior of three different Pd-based BMGs by nanoindentation with high sensitivity and relates it to the structural information gained by electron diffraction. Via the statistical analysis of the first pop-ins during mechanical loading [61], our findings provide strong indications for the activation of two distinct STZ types, each consisting of fewer than 100 atoms [34]. For both STZ types, $(Pd_{40}Ni_{40}P_{20})_{99}Fe_1$ exhibits the largest size while $(Pd_{40}Ni_{40}P_{20})_{99}Co_1$ reveals the smallest. In particular, the plasticity of $(Pd_{40}Ni_{40}P_{20})_{99}Co_1$ has been reported to be significantly higher than that of $(Pd_{40}Ni_{40}P_{20})_{99}Fe_1$ [7,70]. For all three alloys, the activation volume and the STZ size at stresses below a certain critic value τ_C are substantially higher than for higher loading stresses. The size of the corresponding STZ is approximately twice as large as the size of the second fraction. It is apparent that the addition of Co and Fe has had opposite effects on the STZ size, see Table 1. The stress-induced appearance of an additional STZ family indicates an intrinsic heterogeneity of BMGs, which is significantly affected by microalloying. Note that an increase in STZ volume as deduced from nanoindentation correlates with an earlier failure in macroscopic compression or three-point bending tests. of the BMGs [7], probably due to increased stresses required for shear band generation.

The negative strain rate sensitivity of MGs is related to their deformation mechanism. At low strain rates, there may be sufficient time for a diffusive relaxation of the atomic structure to occur following an STZ operation. Following this idea, at the higher strain rates, there might not be adequate time for this relaxation to take place. As a result, the magnitude of mesoscopic flow events during plastic deformation increases, and, as a result, fewer shear bands are formed. Since each pop-in represents a shear event, it is essential to examine the pop-in behavior of the alloys at the specified strain rates as it serves as the primary indicator of shear band formation. In previous studies [28, 32,55], the average pop-in displacement has been used to evaluate the rate dependence of the serrations in the loading curve. However, our observation indicates that although the frequency or number of pop-ins decreases with increasing rate (either in displacement- or load-controlled mode), the depths of the pop-ins are not significantly affected by the rate (see Fig. S8). Therefore, a statistical analysis of the number of pop-in events represents the material's response more accurately.

In Fig. 5, a statistical distribution of the pop-in events vs. the corresponding displacements is shown. To determine the pop-ins quantitatively, a power law function has been fitted to the $p-h$ curve and the pop-ins have been detected based on the resolution (± 0.1) nm of the device. For each composition, 300 indentation curves with strain rates of 0.005, 0.05, and 0.5 $\mu m \cdot s^{-1}$ have been evaluated (see Fig. S8), respectively. Fig. 5(a) shows a comparison of the distribution of pop-ins at the lowest strain rate for the three alloys. Among the three compositions, $(Pd_{40}Ni_{40}P_{20})_{99}Co_1$ exhibits the highest total number of pop-ins, while $(Pd_{40}Ni_{40}P_{20})_{99}Fe_1$ displays significantly lower values. The pop-in distributions at three different strain rates for each composition are shown in Fig. 5(b)–(d). The figure clearly demonstrates a decrease in the number of pop-ins as the strain rate increases for all compositions. In particular, $(Pd_{40}Ni_{40}P_{20})_{99}Co_1$ and $Pd_{40}Ni_{40}P_{20}$ exhibit similar trends, while $(Pd_{40}Ni_{40}P_{20})_{99}Fe_1$ shows a more pronounced decrease in the number of pop-ins.

This observation aligns with the negative strain rate sensitivity and indicates that $(Pd_{40}Ni_{40}P_{20})_{99}Fe_1$, is in fact more influenced by the strain rate, although it should be noted that most pop-ins exhibit small displacements at any applied strain rate.

A smaller STZ size leads to easier activation (a lower activation barrier) of STZ, consequently resulting in conditions that favor the formation of a larger number of shear bands per unit strain, thus explaining the larger number of pop-ins for $(Pd_{40}Ni_{40}P_{20})_{99}Co_1$and its increased macroscopic deformability. The present results support this interpretation; see Table 1 and Fig. 5.

The distinct mechanical responses of the three alloys imply a potential correlation between the mechanical properties and the local atomic structure, offering insights into the structure–property correlations of metallic glasses. In metallic glasses, approximate rotational symmetry has been recognized as a significant characteristic of the local structure [88]. Many metallic glasses exhibit a structure that features some degree of icosahedral local ordering, which is defined by a distinct five-fold rotational symmetry [51]. While five-fold symmetry conflicts with crystalline translational symmetry [50], it is compatible with quasicrystals. This duality could either promote glass formation by inhibiting crystal nucleation or hinder it by favoring quasicrystal nucleation. Furthermore, the compact arrangements associated with the five-fold symmetry implies an intrinsically more brittle glass state rather than a ductile one.

Recent observations suggest that coordinated transformations in the centro-symmetry of local cluster arrangements serve as significant indicators of plastic events [89]. These transformations produce measurable structural parameters derived from the diffraction patterns of glass [90]. Furthermore, the concept of "soft spots" has emerged as an insightful framework for examining the initiation of irreversible rearrangements and plasticity. This framework improves our understanding of newly identified, precisely defined topological defects, particularly vortex-like and antivortex-like defects within the three-dimensional non-affine displacement field [91–95]. These defects seem pivotal in governing the microscopic mechanical behavior and yielding properties of a model three-dimensional glass during shear deformation. Thus,

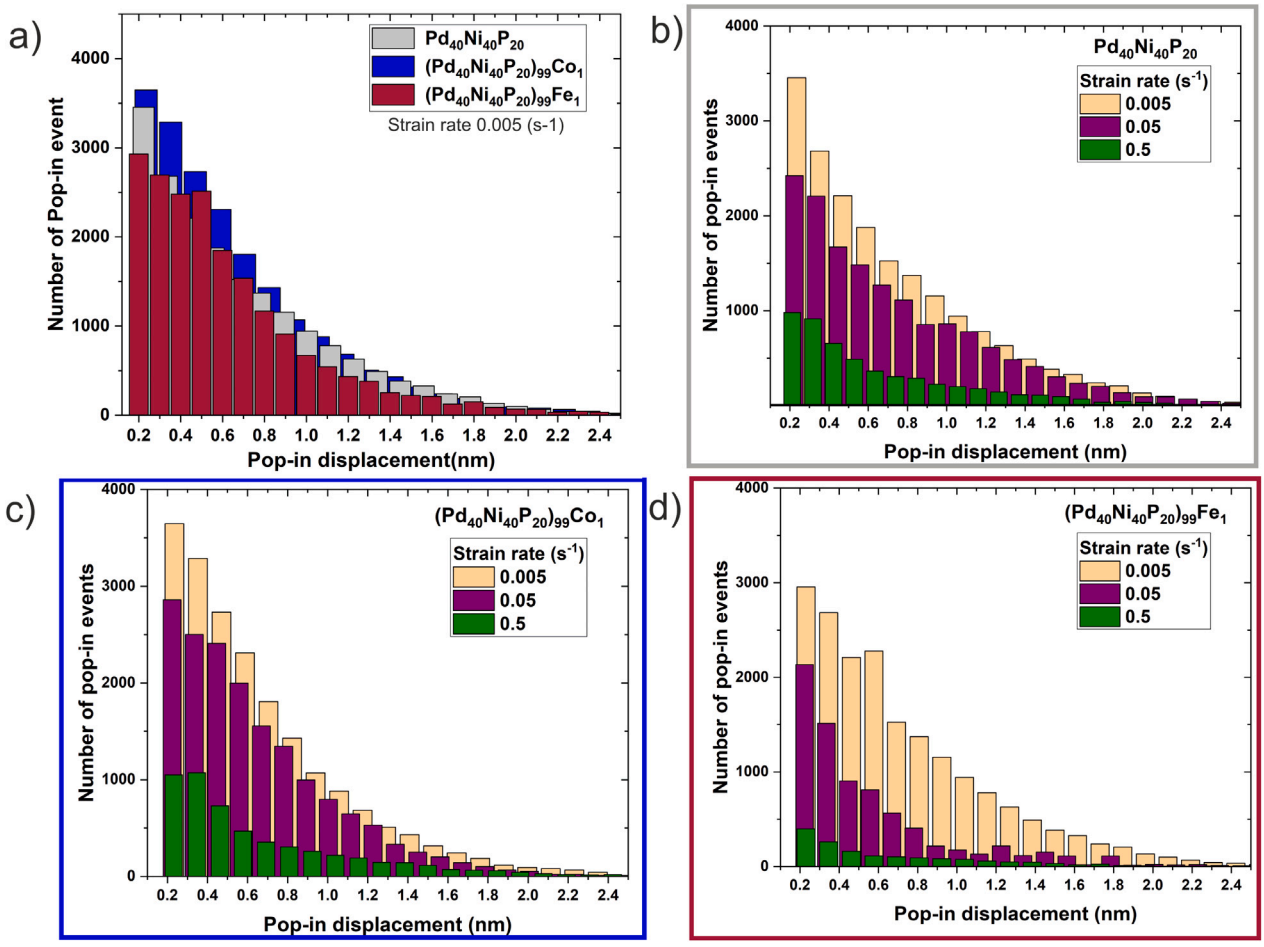

Fig. 5. Distribution of the pop-in frequency in dependence of the pop-in displacement. (a) comparison of the pop-in distribution at the strain rate of 0.005 1/s. (b,c,d) pop-in distribution at different strain rates for the three alloys. It is evident that while for all three compositions, smaller pop-ins are more frequent than large ones, $(Pd_{40}Ni_{40}P_{20})_{99}Co_1$ shows the highest number of smaller pop-ins which may be an indicator for multiple shear band formation and thus enhanced plasticity.

we may hypothesize that the load transfer within the glass is influenced by the spatial arrangement of soft spots, where the level of centro-symmetry of four- and six-fold clusters plays a crucial role in determining plasticity, as suggested by the present symmetry analysis indicated in Fig. 3. The detection of varying amounts and types of symmetry within the same glass highlights the complex relationship between structural motifs and regions that are more readily activated under an applied shear stress, specifically with respect to shear transformation zones (STZs). Although our current understanding of this relationship is still developing and requires targeted, comprehensive studies that integrate experimental analyses and atomistic simulations, the framework of (metallic) glasses consisting of a rigid backbone interspersed with regions exhibiting faster dynamics (i.e. "soft spots") provides a valuable perspective for interpretation [96].

The statistical analysis of the pop-in events in Fig. 5 provides a correlation between the number of pop-ins and the plasticity of the material. It is also in line with the observation of a negative strain rate sensitivity for the three compositions. The strain rate of MGs is proportional to the plastic flow that is localized in shear bands. At higher strain rates, reduced diffusive relaxation results in the activation of fewer shear bands. The decrease in the number of pop-ins in the case of $(Pd_{40}Ni_{40}P_{20})_{99}Fe_1$, which exhibits a higher negative strain rate sensitivity, reflects this phenomenon. While the direct relationship between the cluster symmetry and the STZ remains to be uncovered, the present data suggest that increased fractions of clusters with centro-symmetry may increase the likelihood of multiple shear band formation and thus enhanced plasticity under compression or shear.

With the results of the present analysis, a hypothesis about more detailed structure–property correlations in metallic glasses might also be ventured. For the pristine and the minor alloyed compositions, the MRO has been analyzed by variable resolution fluctuation electron microscopy (VR-FEM) [70]. Distinct differences for the three glassy systems have been observed, that relate the enhanced macroscopic plasticity of the Co-containing glass to a more heterogeneous atomic structure, i.e. a more heterogeneous MRO structure that is characterized by a higher number of dominant motifs. This finding is in line with reports on related as well as different metallic glasses [97–99] and also relates to correlations between MRO and excess free volume in a BMG [100].

5. Conclusions

A pristine $Pd_{40}Ni_{40}P_{20}$ glass and its two variants that were micro alloyed with Co or Fe, respectively, have been synthesized and analyzed with respect to their atomic structure, their pop-in behavior during nanindentation and their strain rate sensitivity. APT analysis substantiates that any clustering of Co or Fe atoms or the formation of Co–Co or Fe–Fe pairs can be ruled out. APT and TEM-based analyses confirm a homogeneous distribution of the elements for all three different alloys. Previous measurements on the identical materials have shown that minor alloying with Co increases the macroscopic plasticity under compression or shear while a minor Fe addition leads to early catastrophic failure. Structural analyses of the same BMGs by VR-FEM showed that higher macroscopic plasticity correlated with a more heterogeneous distribution of local motifs that constitute the respective MRO.

The analysis of the initial pop-in events in the nanoindentation curve has identified two groups of STZs. Notably, the alloy with higher macroscopic plasticity exhibited smaller STZ sizes, whereas the alloy with lower plasticity displayed larger STZ sizes for both groups of STZs. This finding provides valuable insights into the varying plasticity of the alloys, as smaller STZs are more easily activated, thus conceptually leading to the formation of multiple shear bands and thus to an increased plastic deformability in shear or compression before the occurrence of catastrophic failure in a BMG. Furthermore, investigation of strain rate sensitivity and statistical data on pop-in behavior indicates that the $(Pd_{40}Ni_{40}P_{20})_{99}Fe_1$, alloy has the lowest occurrence of pop-ins compared to the other two alloys. Although all three alloys exhibit negative strain rate sensitivity, the $(Pd_{40}Ni_{40}P_{20})_{99}Fe_1$ alloy demonstrates a higher negative value of the strain rate sensitivity.

Additionally, after conducting microstructure analyses, it has been observed that the Co containing alloy, which possesses larger plasticity, displays the highest fraction of centro-symmetric clusters, suggesting the formation of numerous and smaller STZs, ultimately enhancing the plasticity of the material.

Together with the earlier results on the MRO of the three glassy alloys [70], the current results indicate a correlation between the presence and abundance of different local motifs, the prevalence of zones that are activated at low stresses to become STZs and an enhanced macroscopic plasticity. While the correlation between these features does not verify a direct interdependence, the present results may suggest a true structure–property relation in metallic glasses that is based on the distribution of structurally distinct local motifs that may be altered, e.g. by minor alloying. This hypothesis might trigger future work, both experimentally and by atomistic simulations, concerning MRO engineering for obtaining MGs with enhanced performance.

CRediT authorship contribution statement

S. Khademorezaian: Writing – original draft, Visualization, Validation, Software, Methodology, Investigation, Formal analysis, Data curation. **M.W. da Silva Pinto:** Writing – review & editing, Visualization, Validation, Software, Investigation, Formal analysis, Data curation. **M. Peterlechner:** Writing – review & editing, Visualization, Validation, Supervision, Software, Investigation, Formal analysis, Data curation. **H. Rösner:** Writing – review & editing, Visualization, Validation, Supervision, Methodology, Investigation, Funding acquisition, Formal analysis, Data curation. **S.V. Divinski:** Writing – review & editing, Validation, Supervision, Formal analysis, Data curation. **M. Eusterholz:** Writing – review & editing, Visualization, Methodology, Investigation, Formal analysis, Data curation. **G. Wilde:** Writing – review & editing, Supervision, Resources, Project administration, Funding acquisition, Conceptualization.

Declaration of competing interest

The authors declare that they have no known competing financial interests or personal relationships that could have appeared to influence the work reported in this paper.

Acknowledgments

The authors thank the German Research Foundation (DFG) for the financial support via the projects WI 1899/38-1 and WI 1899/47-1. This work was partly carried out with the support of the Karlsruhe Nano Micro Facility (KNMFi, www.knmf.kit.edu), a Helmholtz Research Infrastructure at Karlsruhe Institute of Technology (KIT, www.kit.edu) (proposal 2023-029-031613). Moreover, Dr. Roman Mouginot from FemtoTools is acknowledged for support with the FemtoTools nanoindentation device and fruitful discussions.

Appendix A. Supplementary data

Supplementary material related to this article can be found online at https://doi.org/10.1016/j.jallcom.2025.182099.

References

[1] M.F. Ashby, A.L. Greer, Metallic glasses as structural materials, Scr. Mater. 54 (3) (2006) 321–326, http://dx.doi.org/10.1016/j.scriptamat.2005.09.051.
[2] S. Nowak, P. Ochin, A. Pasko, O. Maciejak, P. Aubert, Y. Champion, Nanoindentation analysis of the mechanical behavior of Zr-based metallic glasses with Sn, Ta and W additions, J. Alloys Compd. 483 (1–2) (2009) 139–142, http://dx.doi.org/10.1016/j.jallcom.2008.07.178.
[3] Z.P. Lu, C.T. Liu, Role of minor alloying additions in formation of bulk metallic glasses: A review, 2004, http://dx.doi.org/10.1023/B:JMSC.0000031478.73621.64.
[4] W.H. Wang, Roles of minor additions in formation and properties of bulk metallic glasses, Prog. Mater. Sci. 52 (4) (2007) 540–596, http://dx.doi.org/10.1016/j.pmatsci.2006.07.003.
[5] J. Eckert, J. Das, S. Pauly, C. Duhamel, Mechanical properties of bulk metallic glasses and composites, J. Mater. Res. 22 (2) (2007) 285–301.
[6] X. Wang, Q.P. Cao, Y.M. Chen, K. Hono, C. Zhong, Q.K. Jiang, X.P. Nie, L.Y. Chen, X.D. Wang, J.Z. Jiang, A plastic Zr-Cu-Ag-Al bulk metallic glass, Acta Mater. 59 (3) (2011) 1037–1047, http://dx.doi.org/10.1016/j.actamat.2010.10.034.
[7] N. Nollmann, I. Binkowski, V. Schmidt, H. Rösner, G. Wilde, Impact of microalloying on the plasticity of Pd-based bulk metallic glasses, Scr. Mater. 111 (2016) 119–122, http://dx.doi.org/10.1016/j.scriptamat.2015.08.030.
[8] Y. Wang, K. Zhang, Y. Feng, Y. Li, W. Tang, Y. Zhang, B. Wei, Z. Hu, Mechanism of local hardening in metallic glass during He Ion irradiation, Materialia 11 (2019) http://dx.doi.org/10.1016/j.mtla.2020.100691.
[9] S. Im, Y. Wang, P. Zhao, G.H. Yoo, Z. Chen, G. Calderon, M.A. Gharacheh, M. Zhu, O. Licata, B. Mazumder, et al., Medium-range ordering, structural heterogeneity, and their influence on properties of Zr-Cu-Co-Al metallic glasses, Phys. Rev. Mater. 5 (11) (2021) 115604.
[10] A.S. Argon, Mechanisms of inelastic deformation in 43 (10).
[11] A.S. Argon, H.Y. Kuo, Plastic flow in a disordered bubble raft (an analog of a metallic glass), Mater. Sci. Eng. 39 (1) (1979) 101–109, http://dx.doi.org/10.1016/0025-5416(79)90174-5.
[12] A.S. Argon, L.T. Shi, Development of visco-plastic deformation in metallic glasses, Acta Metall. 31 (4) (1983) 499–507, http://dx.doi.org/10.1016/0001-6160(83)90038-X.
[13] F. Spaepen, A microscopic mechanism for steady state inhomogeneous flow in metallic glasses, Acta Metall. 25 (4) (1977) 407–415, http://dx.doi.org/10.1016/0001-6160(77)90232-2.
[14] M.L. Falk, J.S. Langer, Dynamics of viscoplastic deformation in amorphous solids, Phys. Rev. E 57 (6) (1998) 7192.
[15] W.L. Johnson, K. Samwer, A universal criterion for plastic yielding of metallic glasses with a (T/Tg)2/3 temperature dependence, Phys. Rev. Lett. 95 (19) (2005) 2–5, http://dx.doi.org/10.1103/PhysRevLett.95.195501.
[16] P.G. Debenedetti, F.H. Stillinger, Supercooled liquids and the glass transition, 2001, http://dx.doi.org/10.1038/35065704.
[17] A. Heuer, Exploring the potential energy landscape of glass-forming systems: from inherent structures via metabasins to macroscopic transport, J. Phys.: Condens. Matter. 20 (37) (2008) 373101.
[18] C. Schuh, T. Nieh, A survey of instrumented indentation studies on metallic glasses, J. Mater. Res. 19 (2004) 46–57.
[19] H. Bei, Z.P. Lu, E.P. George, Theoretical strength and the onset of plasticity in bulk metallic glasses investigated by nanoindentation with a spherical indenter, Phys. Rev. Lett. 93 (12) (2004) 1–4, http://dx.doi.org/10.1103/PhysRevLett.93.125504.
[20] I.C. Choi, Y. Zhao, B.G. Yoo, Y.J. Kim, J.Y. Suh, U. Ramamurty, J.I. Jang, Estimation of the shear transformation zone size in a bulk metallic glass through statistical analysis of the first pop-in stresses during spherical nanoindentation, Scr. Mater. 66 (11) (2012) 923–926, http://dx.doi.org/10.1016/j.scriptamat.2012.02.032.
[21] I.-C. Choi, Y. Zhao, Y.-J. Kim, B.-G. Yoo, J.-Y. Suh, U. Ramamurty, J. i. Jang, Indentation size effect and shear transformation zone size in a bulk metallic glass in two different structural states, Acta Mater. 60 (19) (2012) 6862–6868.
[22] Y. Chen, Z.-X. Bo, H.B. Zhou, B.-A. Sun, Y.H. Sun, R. Maaß, W.H. Wang, Nanoindentation reveals universal scaling of pop-in plasticity in metallic glasses, Scr. Mater. 259 (2025) 116549.
[23] T.F. Page, W.C. Oliver, C.J. McHargue, The deformation behavior of ceramic crystals subjected to very low load (nano)indentations, J. Mater. Res. 7 (2) (1992) 450–473, http://dx.doi.org/10.1557/JMR.1992.0450.
[24] G. Bérces, N.Q. Chinh, A. Juhász, J. Lendvai, Kinematic analysis of plastic instabilities occurring in microhardness tests, Acta Mater. 46 (6) (1998) 2029–2037, http://dx.doi.org/10.1016/S1359-6454(97)00428-X.

[25] D.L. Kohlstedt, The injection of plasticity by M I L L I N E W T O N contacts, 43 (4) (1995) 1569–1576.

[26] V.A. Khonik, A.T. Kosilov, V.A. Mikhailov, The kinetics of stress-oriented structural relaxation in metallic glasses, J. Non-Cryst. Solids 192–193 (1995) 420–423, http://dx.doi.org/10.1016/0022-3093(95)00385-1.

[27] C.A. Schuh, Nanoindentation studies of materials, Mater. Today 9 (5) (2006) 32–40, http://dx.doi.org/10.1016/S1369-7021(06)71495-X.

[28] C.A. Schuh, A.C. Lund, Application of nucleation theory to the rate dependence of incipient plasticity during nanoindentation, J. Mater. Res. 19 (7) (2004) 2152–2158, http://dx.doi.org/10.1557/JMR.2004.0276.

[29] C.A. Schuh, J.K. Mason, A.C. Lund, Quantitative insight into dislocation nucleation from high-temperature nanoindentation experiments, Nat. Mater. 4 (8) (2005) 617–621, http://dx.doi.org/10.1038/nmat1429.

[30] I.C. Choi, Y. Zhao, Y.J. Kim, B.G. Yoo, J.Y. Suh, U. Ramamurty, J.I. Jang, Indentation size effect and shear transformation zone size in a bulk metallic glass in two different structural states, Acta Mater. 60 (19) (2012) 6862–6868, http://dx.doi.org/10.1016/j.actamat.2012.08.061.

[31] Y. Ma, G.J. Peng, T.T. Debela, T.H. Zhang, Nanoindentation study on the characteristic of shear transformation zone volume in metallic glassy films, Scr. Mater. 108 (2015) 52–55, http://dx.doi.org/10.1016/j.scriptamat.2015.05.043.

[32] F. Pöhl, Pop-in behavior and elastic-to-plastic transition of polycrystalline pure iron during sharp nanoindentation, Sci. Rep. 9 (1) (2019) 1–12, http://dx.doi.org/10.1038/s41598-019-51644-5.

[33] K.E. Avila, S. Küchemann, I.A. Alhafez, H.M. Urbassek, Shear-transformation zone activation during loading and unloading in nanoindentation of metallic glasses, Mater. 12 (9) http://dx.doi.org/10.3390/ma12091477.

[34] K. Tao, J. Qiao, Q. He, K. Song, Y. Yang, Revealing the structural heterogeneity of metallic glass: Mechanical spectroscopy and nanoindentation experiments, Int. J. Mech. Sci. 201 (2021) 106469.

[35] J.C. Qiao, J.M. Pelletier, Y. Yao, Creep in bulk metallic glasses. Transition from linear to non linear regime, Mater. Sci. Eng. 743 (2019) 185–189.

[36] D. Sopu, A. Stukowski, M. Stoica, S. Scudino, Atomic-level processes of shear band nucleation in metallic glasses, Phys. Rev. Lett. 119 (2017) 195503.

[37] D. Sopu, STZ-Vortex model: The key to understand STZ percolation and shear banding in metallic glasses, J. Alloys Compd. 960 (2023) 170585.

[38] Y. Mitrofanov, M. Peterlechner, I. Binkowski, M. Zadorozhnyy, I. Golovin, S. Divinski, G. Wilde, The impact of elastic and plastic strain on relaxation and crystallization of Pd–Ni–P-based bulk metallic glasses, Acta Mater. 90 (2015) 318–329, http://dx.doi.org/10.1016/j.actamat.2015.03.001, URL https://www.sciencedirect.com/science/article/pii/S135964541500155X.

[39] B. Riechers, A. Das, R. Rashidi, E. Dufresne, R. Maaß, Metallic glasses: Elastically stiff yet flowing at any stress, Mater. Today 82 (2025) 92–98, http://dx.doi.org/10.1016/j.mattod.2024.11.015, URL https://www.sciencedirect.com/science/article/pii/S1369702124002736.

[40] P.M. Derlet, R. Maaß, Micro-plasticity in a fragile model binary glass, Acta Mater. 209 (2021) 116771.

[41] G. Wilde, G. Görler, R. Willnecker, G. Dietz, Thermodynamic properties of Pd40Ni40P20 in the glassy, Liq. Cryst. States Appl. Phys. Lett. 65 (4) (1994) 397–399.

[42] G. Wilde, G. Görler, R. Willnecker, H. Fecht, Calorimetric, thermomechanical, and rheological characterizations of bulk glass-forming Pd40Ni40P20, J. Appl. Phys. 87 (3) (2000) 1141–1152.

[43] G. Wilde, J. Sebright, J. Perepezko, Bulk liquid undercooling and nucleation in gold, Acta Mater. 54 (18) (2006) 4759–4769.

[44] C. Ophus, Four-dimensional scanning transmission electron microscopy (4d-stem): From scanning nanodiffraction to ptychography and beyond, Microsc. Microanal. 25 (3) (2019) 563–582.

[45] B. Kestel, Non-acid electrolyte thins many materials for tem without causing hydride formation, Ultramicroscopy 19 (2) (1986) 205–211.

[46] J. Duncan, et al., pyxem/pyxem: pyxem 0.15.1. online. http://dx.doi.org/10.5281/zenodo.7927374.

[47] C. Francis, P.M. Voyles, Pyxem: A scalable mature Python package for analyzing 4-d stem data, 2023.

[48] D.N. Johnstone, P. Crout, J. Laulainen, S. Høgås, B. Martineau, T. Bergh, S. Smeets, S. Collins, J. Morzy, H. Ånes, et al., Pyxem/pyxem: Pyxem 0.10. 0, 2020.

[49] S. Huang, C. Francis, J. Ketkaew, J. Schroers, P.M. Voyles, Correlation symmetry analysis of electron nanodiffraction from amorphous materials, Ultramicroscopy 232 (2022) 113405.

[50] D.B. Miracle, A structural model for metallic glasses, Nat. Mater. 3 (10) (2004) 697–702, http://dx.doi.org/10.1038/nmat1219.

[51] S. Sachdev, D. Nelson, Order in metallic glasses and icosahedral crystals, Phys. Rev. B 32 (7) (1985) 4592.

[52] K. Thompson, D. Lawrence, D. Larson, J. Olson, T. Kelly, B. Gorman, In situ site-specific specimen preparation for atom probe tomography, Ultramicroscopy 107 (2–3) (2007) 131–139.

[53] H. Li, G. Subhash, X.-L. Gao, L.J. Kecskes, R.J. Dowding, Negative strain rate sensitivity and compositional dependence of fracture strength in Zr/Hf based bulk metallic glasses, Scr. Mater. 49 (11) (2003) 1087–1092.

[54] F.H. DallaTorre, A. Dubach, M.E. Siegrist, J.F. Löffler, Negative strain rate sensitivity in bulk metallic glass and its similarities with the dynamic strain aging effect during deformation, Appl. Phys. Lett. 89 (9) (2006) 1–4, http://dx.doi.org/10.1063/1.2234309.

[55] A. Bhattacharyya, G. Singh, K. Eswar Prasad, R. Narasimhan, U. Ramamurty, On the strain rate sensitivity of plastic flow in metallic glasses, Mater. Sci. Eng. 625 (2015) 245–251, http://dx.doi.org/10.1016/j.msea.2014.12.004.

[56] M.C. Weinberg, Thermochimica acta Glass-formation and crystallization kinetics 1, Thermochim. Acta 280 (1996) 63–71.

[57] B.P. Sahu, A. Dutta, R. Mitra, Mechanism of negative strain rate sensitivity in metallic glass film, J. Alloys Compd. 784 (2019) 488–499.

[58] K.L. Johnson, K.L. Johnson, Contact Mechanics, Cambridge University Press, 1987.

[59] W.C. Oliver, G.M. Pharr, An improved technique for determining hardness and elastic madulus using load and displacement, J. Mater. Res. 7 (1) (1992) 1564–1583.

[60] D. Pan, A. Inoue, T. Sakurai, M.W. Chen, Experimental characterization of shear transformation zones for plastic flow of bulk metallic glasses, Proc. Natl. Acad. Sci. USA 105 (39) (2008) 14769–14772, http://dx.doi.org/10.1073/pnas.0806051105.

[61] L. Perriere, S. Nowak, S. Brossard, M.-T. Thai, M. Bletry, Y. Champion, Nanoindentation study of chemical effects on the activation volume controlling shear band initiation in metallic glasses, Scr. Mater. 68 (3–4) (2013) 183–186.

[62] M. Atzmon, J.D. Ju, Microscopic description of flow defects and relaxation in metallic glasses, Phys. Rev. Stat. Nonlinear Soft Matter Phys. 90 (4) (2014) 1–6, http://dx.doi.org/10.1103/PhysRevE.90.042313.

[63] N. Thurieau, L. Perrière, M. Laurent-Brocq, Y. Champion, Activation volume in heterogeneous deformation of Mg65Cu12.5Ni12.5(Ce75La25)10 metallic glass, J. Appl. Phys. 118 (20) (2015) 10–15, http://dx.doi.org/10.1063/1.4936220.

[64] T. Lei, L.R. DaCosta, M. Liu, J. Shen, Y. Sun, W. Wang, M. Atzmon, Composition dependence of metallic glass plasticity and its prediction from anelastic relaxation–A shear transformation zone analysis, Acta Mater. 195 (2020) 81–86.

[65] J.H. Perepezko, S.D. Imhoff, M.W. Chen, J.Q. Wang, S. Gonzalez, Nucleation of shear bands in amorphous alloys, Proc. Natl. Acad. Sci. USA 111 (11) (2014) 3938–3942, http://dx.doi.org/10.1073/pnas.1321518111.

[66] P. Saini, S. Nag, J. i. Jang, I.C. Choi, U. Ramamurty, R.L. Narayan, A statistical analysis of the second 'pop-in' behaviour of the spherical-tip nanoindentation of Zr-based bulk metallic glasses, Materialia 31 (2023) 101862, http://dx.doi.org/10.1016/j.mtla.2023.101862.

[67] S. Nag, R.L. Narayan, J.I. Jang, C. Mukhopadhyay, U. Ramamurty, Statistical nature of the incipient plasticity in amorphous alloys, Scr. Mater. 187 (2020) 360–365, http://dx.doi.org/10.1016/j.scriptamat.2020.06.045.

[68] M.J. Mayo, W.D. Nix, A micro-indentation study of superplasticity in Pb, Sn, and Sn-38 wt% Pb, Acta Metall. 36 (8) (1988) 2183–2192, http://dx.doi.org/10.1016/0001-6160(88)90319-7.

[69] B.N. Lucas, W.C. Oliver, Indentation power-law creep of high-purity indium, Met. Mater. Trans. Phys. Met. Mater. Sci. 30 (3) (1999) 601–610, http://dx.doi.org/10.1007/s11661-999-0051-7.

[70] S. Hilke, H. Rösner, G. Wilde, The role of minor alloying in the plasticity of bulk metallic glasses, Scr. Mater. 188 (2020) 50–53, http://dx.doi.org/10.1016/j.scriptamat.2020.06.070.

[71] M.P. Moody, L.T. Stephenson, A.V. Ceguerra, S.P. Ringer, Quantitative binomial distribution analyses of nanoscale like-solute atom clustering and segregation in atom probe tomography data, Microsc. Res. Tech. 71 (7) (2008) 542–550.

[72] H.B. Yu, W.H. Wang, H.Y. Bai, Y. Wu, M.W. Chen, Relating activation of shear transformation zones to β relaxations in metallic glasses, Phys. Rev. B 81 (2010) 220201.

[73] H.B. Yu, W.H. Wang, K. Samwer, The β relaxation in metallic glasses: An overview, Mater. Today 16 (2013) 183–191.

[74] Q. Wang, J.J. Liu, Y.F. Ye, T.T. Liu, S. Wang, C.T. Liu, J. Lu, Y. Yang, Universal secondary relaxation and unusual brittle-to-ductile transition in metallic glasses, Mater. Today 20 (2017) 293–300.

[75] J.C. Qiao, Q. Wang, J.M. Pelletier, H. Kato, R. Casalini, D. Crespo, E. Pineda, Y. Yao, Y. Yang, Structural heterogeneities and mechanical behavior of amorphous alloys, Prog. Mater. Sci. 104 (2019) 250–329.

[76] G. Kumar, D. Rector, R.D. Conner, J. Schroers, Embrittlement of Zr-based bulk metallic glasses, Acta Mater. 57 (2009) 3572–3583.

[77] G. Kumar, S. Prades-Rodel, A. Blatter, J. Schroers, Unusual brittle behavior of Pd-based bulk metallic glass, Scr. Mater. 65 (2011) 585–587.

[78] W.H. Wang, Dynamic relaxations and relaxation-property relationships in metallic glasses, Prog. Mater. Sci. 106 (2019) 100561.

[79] G. Kumar, P. Neibecker, Y.H. Liu, J. Schroers, Critical fictive temperature for plasticity in metallic glasses, Nat. Commun. 4 (2013) 1536.

[80] A.Q. Tool, C.G. Eichlin, Variations caused in the heating curves of glass by heat treatment, J. Am. Ceram. Soc. 14 (1931) 276–308.

[81] C.E. Packard, L.M. Witmer, C.A. Schuh, Hardening of a metallic glass during cyclic loading in the elastic range, Appl. Phys. Lett. 92 (2008) 171911.

[82] W.H. Wang, The elastic properties, elastic models and elastic perspectives of metallic glasses, Prog. Mater. Sci. 57 (2012) 487–656.

[83] P. Ross, S. Küchemann, P.M. Derlet, H.B. Yu, W. Arnold, P. Liaw, K. Samwer, R. Maaß, Linking macroscopic rejuvenation to nano-elastic fluctuations in a metallic glass, Acta Mater. 138 (2017) 111–118.
[84] A.H. Balal, X.L. Bian, D.X. Han, B. Huang, S.S. Liao, N. Li, S. Ali, Y.D. Jia, J.C. Qiao, G. Wang, The role of cryogenic treatment in the relaxation behavior of the elastically rejuvenated metallic glasses, Int. J. Plast. 189 (2025) 104356.
[85] S.V. Ketov, Y.H. Sun, S. Nachum, Z. Lu, A. Checchi, A.R. Beraldin, H.Y. Bai, W.H. Wang, D.V. Louzguine-Luzgin, M.A. Carpenter, A.L. Greer, Rejuvenation of metallic glasses by non-affine thermal strain, Nat. 524 (2015) 200–203.
[86] X.L. Bian, D. Zhao, J.T. Kim, D. Şopu, G. Wang, R. Pippan, J. Eckert, Controlling the distribution of structural heterogeneities in severely deformed metallic glass, Mater. Sci. Eng. 752 (2019) 36–42.
[87] L.T. Stephenson, M.P. Moody, P.V. Liddicoat, S.P. Ringer, New techniques for the analysis of fine-scaled clustering phenomena within atom probe tomography (apt) data, Microsc. Microanal. 13 (6) (2007) 448–463.
[88] P.J. Steinhardt, D.R. Nelson, M. Ronchetti, Bond-orientational order in liquids and glasses, Phys. Rev. B 28 (2) (1983) 784.
[89] D. Ruan, S. Patinet, M.L. Falk, Predicting plastic events and quantifying the local yield surface in 3d model glasses, J. Mech. Phys. Solids 158 (2022) 104671, http://dx.doi.org/10.1016/j.jmps.2021.104671, URL https://www.sciencedirect.com/science/article/pii/S0022509621003008.
[90] A.C. Liu, H. Pham, A. Bera, T.C. Petersen, T.W. Sirk, S.T. Mudie, R.F. Tabor, J. Nunez-Iglesias, A. Zaccone, M. Baggioli, Measurable geometric indicators of local plasticity in glasses. arXiv preprint arXiv:2410.09391.
[91] Z.W. Wu, Y. Chen, W.-H. Wang, W. Kob, L. Xu, Topology of vibrational modes predicts plastic events in glasses, Nat. Commun. 14 (1) (2023) 2955.
[92] J. Dong, H. Peng, H. Wang, Y. Tong, Y. Wang, W. Dmowski, T. Egami, B. Sun, W. Wang, H. Bai, Non-affine atomic rearrangement of glasses through stress-induced structural anisotropy, Nat. Phys. 19 (12) (2023) 1896–1903.
[93] P. Desmarchelier, S. Fajardo, M.L. Falk, Topological characterization of rearrangements in amorphous solids, Phys. Rev. E 109 (5) (2024) L053002.
[94] A. Bera, M. Baggioli, T.C. Petersen, T.W. Sirk, A.C. Liu, A. Zaccone, Clustering of negative topological charges precedes plastic failure in 3d glasses, PNAS Nexus 3 (9) (2024) pgae315.
[95] V. Vaibhav, A. Bera, A.C. Liu, M. Baggioli, P. Keim, A. Zaccone, Experimental identification of topological defects in 2d colloidal glass, Nat. Commun. 16 (1) (2025) 55.
[96] H. Zhou, X. Jing, L. Yu, G. Ding, S. Cai, C. Shi, L. Dai, M. Jiang, G. Wilde, On the plasticity and inheritance in shear-band-rejuvenated metallic glasses, Intermet. 180 (2025) 108685.
[97] F.A. Davani, S. Hilke, H. Rösner, D. Geissler, A. Gebert, G. Wilde, Correlations between the plasticity and medium-range order of bulk metallic glasses, J. Appl. Phys. 128 (1).
[98] H. Voigt, N. Neuber, O. Vaerst, M. Demming, R. Busch, M. Peterlechner, H. Rösner, G. Wilde, Differences in structure and dynamics of ternary Pd–Ni-based bulk metallic glasses containing sulfur or phosphorous, Acta Mater. 264 (2024) 119574.
[99] N. Grund, D. Holland-Moritz, S. Khademorezaian, L.P. Kreuzer, N. Neuber, L.M. Ruschel, H. Voigt, J. Wilden, F. Yang, S. Banerjee, et al., Impact of sulfur addition on the structure and dynamics of Ni–Nb alloy melts, APL Mater. 12 (5).
[100] S. Khademorezaian, M. Tomut, M. Peterlechner, M. da Silva Pinto, H. Rösner, S. Divinski, G. Wilde, Extreme rejuvenation of a bulk metallic glass at the nanoscale by swift heavy Ion irradiation, J. Alloys Compd. 980 (2024) 173571.